

## ***Allium sativum* extract mediated synthesis of Ag/Zn bimetallic nanostructures for antibacterial application**

E. K. Balcha<sup>a</sup>, A. Marica<sup>b,#</sup>, T. D. Zeleke<sup>a,#,\*</sup>, H. C. A. Murthy<sup>a</sup>, A. Roy<sup>c</sup>,  
C. R. Ravikumar<sup>d</sup>, S. Cavalu<sup>b</sup>, A. K. Azad<sup>e</sup>

<sup>a</sup>Department of Applied Chemistry, School of Applied Natural Science, Adama Science and Technology University, Adama, Ethiopia

<sup>b</sup>Faculty of Medicine and Pharmacy, Doctoral School of Biomedical Sciences, University of Oradea, P-ta 1 Decembrie 10, 410073 Oradea, Romania

<sup>c</sup>Department of Biotechnology, School of Engineering & Technology, Sharda University, Greater Noida, India

<sup>d</sup>Research Centre, Department of Science, East West Institute of Technology, Bangalore 560091, India

<sup>e</sup> Faculty of Pharmacy, MAHSA University, Bandar Saujana Putra, 42610 Jenjarom, Selangor, Malaysia

In this study, Ag and Ag/Zn bimetallic nanostructures (BMNs) were synthesized via the green route by using the extracts of *Allium Sativum L* plant. The obtained structures were characterized for structural, morphological and optical features by using X-ray diffraction (XRD), electron microscopy (SEM) and UV-vis spectroscopy. The XRD results confirmed cubic crystal structure for the Ag/Zn BMNs with average crystallite size 17.47 nm, while for Ag Ns an average crystallite size of 9.31 nm was noticed. UV-vis spectra of Ag and Ag/Zn BMNs showed absorbance maxima at 402 nm and 360 nm, respectively, while the morphological featured recorded by SEM showed irregular shape for both structures. The antibacterial activities of Ag and Ag/Zn bimetallic structures were investigated against selected bacterial strains, the maximum inhibition being recorded against *P. aeruginosa*. In addition, the antibacterial effect was found to increase with increased concentration of both Ag and Ag/Zn nanostructures, while a superior effect was noticed for Ag Ns compared to Ag/Zn BMNs for both the gram-negative and gram-positive bacterial strains.

(Received April 19, 2022; Accepted September 19 2022)

**Keywords:** Ag/Zn bimetallic structures, green synthesis, *Allium Sativum* extract, Antibacterial activity

### **1. Introduction**

The green synthesis and antibacterial applications of metal and metal oxides nanostructures have received a significant attention in recent years due to their capacity to act as an alternative to traditional antibiotics for killing disease causing pathogens [1-3]. The small size and high surface to volume ratio of nanostructures allow them to closely interact with bacterial cells. The high surface area of small size particles also accompanies the release of free metal ions which causes to bacterial inactivation followed by death [4]. The biogenic synthesis of metallic nanostructures find application in photocatalysis, electrocatalysis, bioremediation and bioleaching since many decades [5-8]. The Ag nanostructures such as nanoparticles, nanocrystals, nanorods, nanotubes, nanosheets exhibit versatile properties and hence found to exhibit inhibitory activity against many microorganisms and bacterial strains. The safety of Ag nanostructures on human health rises a great concern among researchers. However, their toxicity of was found to depend on numerous morphological and physicochemical properties of the nanostructures such as the

---

\* Corresponding author: tegened@yahoo.com

# Authors with equal contribution

<https://doi.org/10.15251/DJNB.2022.173.1057>

morphological features, the coating phytoconstituents or coupling with another metal (for example Zn) which may decrease the risk of cytotoxicity [5,6]. Thus, we proposed in this paper the synthesis of mono and bimetallic Ag-Zn nanostructures for antibacterial applications. According to literature, bimetallic nanostructures structures (BMNs) possess superior properties compared to monometallic ones due to their enhanced electronic, optical and catalytic performances [7-9]. Application of plant extracts to synthesize the metallic as well as bimetallic nanostructures has been found very attractive these days. This method is very safe, simple and environment friendly. A large number of plants and their parts were utilized to synthesize BMNs. It is expected that the phytochemicals present in the extracts of plant parts are serving the dual purpose of reducing and stabilizing agents. Many bimetallic nanostructures such as silver-gold, silver-copper, copper-nickel and iron-nickels have been reported recently [8,9]. Different bimetallic structures such as Cu-Ni, Cu-Co, Fe-Pd, Cu-In have been applied for multifunctional applications, but only few reports were found with respect to the green Ag-Zn BMNs and their applications towards biomedical applications [8]. This work was proposed to synthesize Ag-Zn BMNs using the extracts of *Allium Sativum* L plant and further characterize from physico-chemical point of view and antibacterial activity.

## **2. Materials and methods**

### **2.1. Chemicals and reagents**

The chemicals and reagents required for the preparation of Ag Ns and Ag/Zn BMNs were distilled water, zinc nitrate hexahydrate ( $\text{Zn}(\text{NO}_3)_2 \cdot 6\text{H}_2\text{O}$ ), silver nitrate ( $\text{AgNO}_3$ ), ethanol, Dimethyl sulfoxide (DMSO). All the chemicals were of analytical grade and commercially available from Sigma Aldrich, while the garlic plant was purchased from local market. The following bacterial strains were considered for the antibacterial tests: *E. coli* ATCC 25922, *P. aeruginosa* ATCC 27853, *S. aureus* ATCC 29213, *S. pyogenes* CCUG 25571 using disc diffusion method (Mueller-Hinton Agar). The specific reagents used for phytochemical qualitative analysis are mentioned in the section 2.7.

### **2.2. Preparation of the Garlic Plant Extract**

Garlic (*Allium sativum* L.) plant was collected from a local market. The plant was washed several times with tap water and with distilled water and then its skin was peeled off and dried in light at room temperature. The cleaned dried plant was cut and ground to make powder before using it for the synthesis of NPs. 100 g of garlic (*Allium sativum* L) plant powder was added into 1000 mL conical flask containing 600 mL of distilled water; then the mixture was heated to 40 °C for 30 min. After 30 min, the heater was turned off and the mixtures were stirred for 1 h as shown in Figure 1. After a while, the mixture was allowed to settle. Then, after settlement, the extract was filtered with Whatman No 1 filter paper to get the extract for further experiments [10].

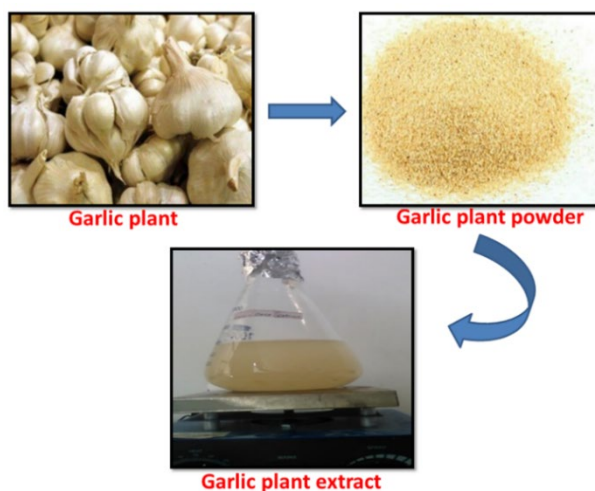


Fig. 1. Preparation of garlic extract and garlic powder.

### 2.3. Green Synthesis of Silver NPs

The synthesis of Ag Ns was accomplished by mixing 500 mL of 0.1 M  $\text{AgNO}_3$  solution and 100 mL of garlic plant extract in 1000 mL of beaker. Later, this mixture was heated to 40 °C for 60 minutes on the hot plate, while continuous stirring. After cooling, the mixture was decanted and centrifuged for 30 min at 10000 rpm. Finally, the solid part was washed with distilled water and ethanol, then dried on a ceramic crucible for 5 days at room temperature. As depicted in Figure 2, the Ag powder was obtained [11].

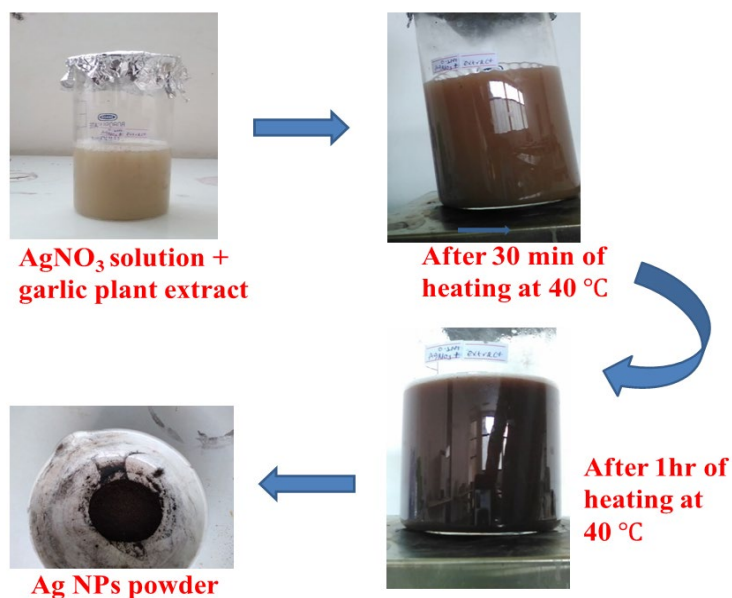


Fig. 2. A schematic presentation of the green synthesis of silver nanoparticles.

### 2.4. Green Synthesis of Ag/Zn BMNs

The green synthesis of Ag/Zn BMNs was carried out by using a mixture containing 0.1 M  $\text{AgNO}_3$ , 0.1M  $\text{ZnNO}_3$  solution and garlic plant extract. 300 mL of 0.1 M  $\text{Zn}(\text{NO}_3)_2$  solution was added to the 1000 mL beaker heated at 40 °C for 15 min. Then, 300 mL of 0.1 M  $\text{AgNO}_3$  solution was added to the beaker while heating and stirring for 15 min. After 15 min the heater was removed. Next, 100 mL of plant extract was added to the solution, drop-wise, with constant stirring for 1 h. The mixture was kept for the formation of the precipitate and centrifuged for 30

min. Finally, the solid precipitate was washed with distilled water and ethanol and dried on a ceramic crucible for 5 days at room temperature. The black powder Ag/Zn BMNs was collected and grounded to get fine powder [12,13].

### **2.5. Characterization Techniques**

Both AgNs and Ag/Zn BMNs were characterized for their crystalline features by X-ray diffractometer (Rigaku Miniflex, Cu-K $\alpha$  radiation) operating at a voltage of 40 kV and applied current of 30 mA, scanning speed of 3.00 degrees per minutes. The UV-Vis absorption spectra were obtained (range of 200–800 nm) by UV-Vis spectrometer (Double beam S-160 spectrophotometer). Chemical bonding interactions were evidenced by using FTIR Spectrophotometer (Perkin Elmer, Spectrum 65 FT-IR, range of 4000-400 cm<sup>-1</sup>). The morphological features were determined by scanning electron microscopy (SEM JEOL, JCM-6000Plus).

### **2.6. Evaluation of antibacterial activity**

The antibacterial activities of the Ag Ns and Ag/Zn BMNs against gram-negative species (*E. coli* and *P. aeruginosa*) and gram-positive species (*S. pyogenes* and *S. aureus*) were evaluated by the disc diffusion agar method. Bacterial species were grown aerobically in the presence of oxygen in nutrient broth for 24 h at 37 °C before using as a target organism. Ag Ns and Ag/Zn BMNs were dispersed in 50 mL of DMSO with continuous stirring for 30 min. Various concentrations of the tested materials (100  $\mu\text{g/mL}$ , 50  $\mu\text{g/mL}$ , 25  $\mu\text{g/mL}$  and 12.5  $\mu\text{g/mL}$ ) were poured using a micro pipette in each pathogen well, after inoculation and cultivation of applied target bacterial on top of Mueller Hinton agar. Finally, the zones of the inhibition were measured in millimeters after 24 h of incubation time [14,15].

### **2.7. Phytochemical Qualitative Analysis**

The plant extracts, methanolic and ethanolic aqueous solutions were assessed for their phytochemical profile, by using the following standard methods [16,17].

#### **2.7.1. Test for Anthraquinones**

10 ml of benzene was added in 6 g of the Ephedra powder sample in a conical flask and soaked for 10 minutes and then filtered. Further 10 ml of 10% ammonia solution was added to the filtrate and shaken vigorously for 30 seconds and pink, violet, or red color indicated the presence of anthraquinones in the ammonia phase.

#### **2.7.2. Test for Tannins**

10 ml of bromine water was added to the 0.5 g aqueous extract. Discoloration of bromine water showed the presence of tannins.

#### **2.7.3. Test for Saponins**

5.0 ml of distilled water was mixed with aqueous crude plant extract in a test tube and it was mixed vigorously. The frothing was mixed with few drops of olive oil and mixed vigorously and the foam appearance showed the presence of saponins.

#### **2.7.4. Tests for Flavonoids (Shinoda Test)**

Pieces of magnesium ribbon and HCl concentrated were mixed with aqueous crude plant extract after few minutes and pink color showed the presence of flavonoid.

Alkaline Reagent Test: 2 ml of 2.0% NaOH mixture was mixed with aqueous plant crude extract; concentrated yellow color was produced, which became colorless when we added 2 drops of diluted acid to mixture, showing the presence of flavonoids.

#### **2.7.5. Tests for Glycosides**

Liebermann's Test: 2.0 ml of acetic acid and 2 ml of chloroform were added to whole aqueous plant crude extract. The mixture was then cooled and H<sub>2</sub>SO<sub>4</sub> concentrated was added. Green color showed the entity of aglycone, steroidal part of glycosides.

**Keller-Kiliani Test:** A solution of glacial acetic acid (4.0 ml) with 1 drop of 2.0% FeCl<sub>3</sub> mixture was mixed with the 10 ml aqueous plant extract and 1 ml H<sub>2</sub>SO<sub>4</sub> concentrated. A brown ring formed between the layers which showed the entity of cardiac steroidal glycosides.

**Salkowski's Test.** We added 2 ml of concentrated H<sub>2</sub>SO<sub>4</sub> to the whole aqueous plant crude extract. A red- brown color formed which indicated the presence of steroidal aglycone part of the glycoside.

#### **2.7.6. Test for Terpenoids**

2.0 ml of chloroform was added with the 5 ml aqueous plant extract and evaporated on the water path and then boiled with 3 ml of H<sub>2</sub>SO<sub>4</sub> concentrated. A grey color formed which showed the entity of terpenoids.

#### **2.7.7. Test for Steroids**

2 ml of chloroform and concentrated H<sub>2</sub>SO<sub>4</sub> were added with the 5 ml aqueous plant crude extract. In the lower chloroform layer red color appeared that indicated the presence of steroids.

#### **2.7.8. Test for Alkaloids**

To about 3 ml of sample solution, a few drops of Wagner's reagent are added. Formation of the brownish precipitate, confirms the presence of alkaloids.

### **3. Results and discussions**

The synthesis of Ag Ns and Ag/Zn BMNs by the use of garlic (*Allium sativum* L.) plant extract has been successful. It is well established that the phytochemicals of the plant extract do reduce Ag<sup>+</sup> and Zn<sup>2+</sup> metal ions and nucleate Ag and Zn atoms to form clusters while Ag and Ag/Zn Ns are stabilized by the phytochemicals. The phytochemical screening has been carried out to explore the nature of biomolecules present in the garlic (*Allium sativum* L.) plant extract.

#### **3.1. Phytochemical screening of plant extract**

The phytochemical screening of the garlic (*Allium sativum* L.) extract revealed the presence of flavonoids, tannins, terpenoids, glycosides, phytosterols, saponins and phenols. These biomolecules are responsible for the reduction and stabilization of Ag and Ag/Zn BMNs. The list of phytochemicals present in the extract is as shown in Table 1. The tests conducted also confirmed the absence of alkaloids, steroids and anthraquinones.

*Table 1. The result of phytochemical screening of Allium sativum L plant.*

No	Secondary Metabolite	Result
1	Flavonoid	+
2	Alkaloid	-
3	Tannins	+
4	Terpenoid	+
5	Steroid	-
6	Glycosides	+
7	Phytosterols	+
8	Anthraquinones	-
9	Saponins	+
10	Phenol	+

### 3.2. Characterization of Ag and Ag/Zn BMNs

The as-synthesized Ag Ns and Ag/Zn BMNs were subjected to characterization by using UV-visible, XRD, FT-IR and SEM techniques to explore their optical, structural, surface bonding and morphological features respectively.

#### 3.2.1. XRD analysis

The XRD analysis emphasize the crystalline size, lattice parameters, micro-strains and dislocation densities of the synthesized Ag and Ag/Zn BMNs, in addition to structural details. The XRD patterns of Ag and Ag/Zn BMNs are shown in Figure 3. For Ag Ns the diffraction patterns were observed at  $2\theta$  values  $38.38^\circ$ ,  $44.23^\circ$ ,  $64.60^\circ$  and  $77.58^\circ$  which corresponds to (111), (200), (220) and (311) plane respectively and cubic phase, according to JCPDS card No. 004-0783. The presence of sharp and intense peaks suggests a high crystallinity. As per the report by Jha & Prasad [21], Ag NPs XRD pattern correspond to the space group Fm-3m, which is in concordance with our results.

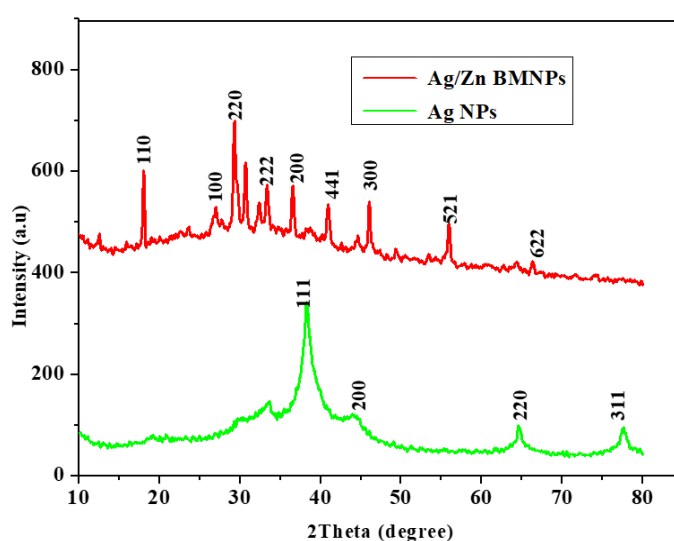


Fig. 3. XRD patterns of Ag and Ag/Zn BMNs.

The XRD patterns of Ag/Zn BMNs shows the peaks at  $2\theta$  values of  $29.36^\circ$ ,  $33.38^\circ$ ,  $40.95^\circ$  and  $55.91^\circ$  which are indexed to (220), (222), (441) and (521) respectively. The spectral data obtained depicted that the synthesized Ag/Zn BMNs showed cubic crystal structure phase and the observed peaks were fitted with the JCPDS card No. 026-0956, space group I-43m. The sharp and intense peaks observed in the XRD spectra indicate a good crystalline feature. The average crystallite size was estimated by using Scherrer's formula (equation 1).

$$D = K\lambda / \beta \cos \theta \quad (1)$$

where

D = mean size of the crystalline domains,

K = dimensionless shape factor with a value close to unity,

$\lambda$  = X-ray wavelength,

$\beta$  = line broadening full width at half maximum intensity (FWHM) in radians,

$\theta$  = Bragg's angle of diffraction.

The dislocation densities of synthesized NPs are calculated using equation 2:

$$\delta = \frac{1}{D^2} \quad (2)$$

where  $\delta$  is the dislocation density,  $D$  is the crystallite size.

The micro-strain is estimated from the equation:

$$\varepsilon = \frac{\beta}{4 \tan \theta} \quad (3)$$

The value of lattice parameter is calculated for hexagonal crystal structure, using the equation:

$$\frac{1}{d^2 hkl} = \frac{4}{3a^2} \times (h^2 + hk + k^2) + \frac{l^2}{c^2} \quad (4)$$

where  $d$  = d-spacing,  $(h,k,l)$  = Miller indices and  $a, c$  = lattice parameter.

For the synthesized Ag Ns and Ag/Zn BMNs, interplanar spacing ( $d$ ), particle size ( $D$ ), dislocation density ( $\delta$ ) and microstrain ( $\varepsilon$ ) were calculated using equations (1- 4) and presented in Table 2 and Table 3. The average crystallite size of the Ag and Ag/Zn BMNs were found to be 9.31 nm and 17.47 nm respectively. The lattice parameter was calculated using the equation (4); since the synthesized materials are cubic in structure, the calculated lattice parameters ( $a = c$ ) are equal.

Table 2. The calculated parameters for the strongest peaks of AgNs.

$2\theta$ (deg)	$\theta$ (deg)	FWHM (deg)	$\beta$ (rad)	$d$ ( $A^\circ$ )	D (nm)	$\delta \times 10^{-3}(nm^{-2})$	$\varepsilon \times 10^{-3}$
38.38	19.19	1.34	0.023	2.34	6.30	25.20	16.75
44.23	22.11	1.52	0.026	2.04	5.64	31.44	16.31
64.60	32.30	0.77	0.013	1.44	12.20	6.72	5.32
77.54	38.77	0.78	0.013	1.23	13.11	5.81	4.23

Table 3. The calculated parameters for the strongest peaks of Ag/Zn Ns.

$2\theta$ (deg)	$\theta$ (deg)	FWHM (deg)	$\beta$ (rad)	$d$ ( $A^\circ$ )	D (nm)	$\delta \times 10^{-3}(nm^{-2})$	$\varepsilon \times 10^{-3}$
29.36	14.68	0.54	0.0093	3.04	15.36	4.24	8.91
33.38	16.69	0.48	0.0084	2.68	17.19	3.39	7.04
40.95	20.47	0.47	0.0083	2.20	17.87	3.13	5.55
55.91	27.95	0.46	0.0081	1.64	19.47	2.64	3.80

The decrease in the microstrain ( $\varepsilon$ ) is correlated to the increased angle ( $2\theta$ ) or peak position. The average crystallite size was found to increase as the peak position decreases corroborating that the crystallite size also contributes to peak broadening phenomenon. Dislocation

density measures the number of dislocations in a unit volume of crystalline materials. Thus, it can be concluded that, as particle size increases, the dislocation density of the crystalline materials decreases. In another word, as the peak position (angle) increases, the dislocation density of the crystallite/particle also increases. When the synthesized nanostructures were compared, the synthesized Ag Ns and Ag/Zn BMNs exhibited an average crystallite size of 9.31 nm and 17.47 nm respectively, since the dislocation density depends upon the particle size.

### 3.2.2. UV- vis spectroscopy analysis

Figure 4(a-c) depicts the absorption and transmittance spectra of Ag Ns, while Figure 5(a-c) presents the absorption and transmittance spectra of Ag/Zn BMNs.

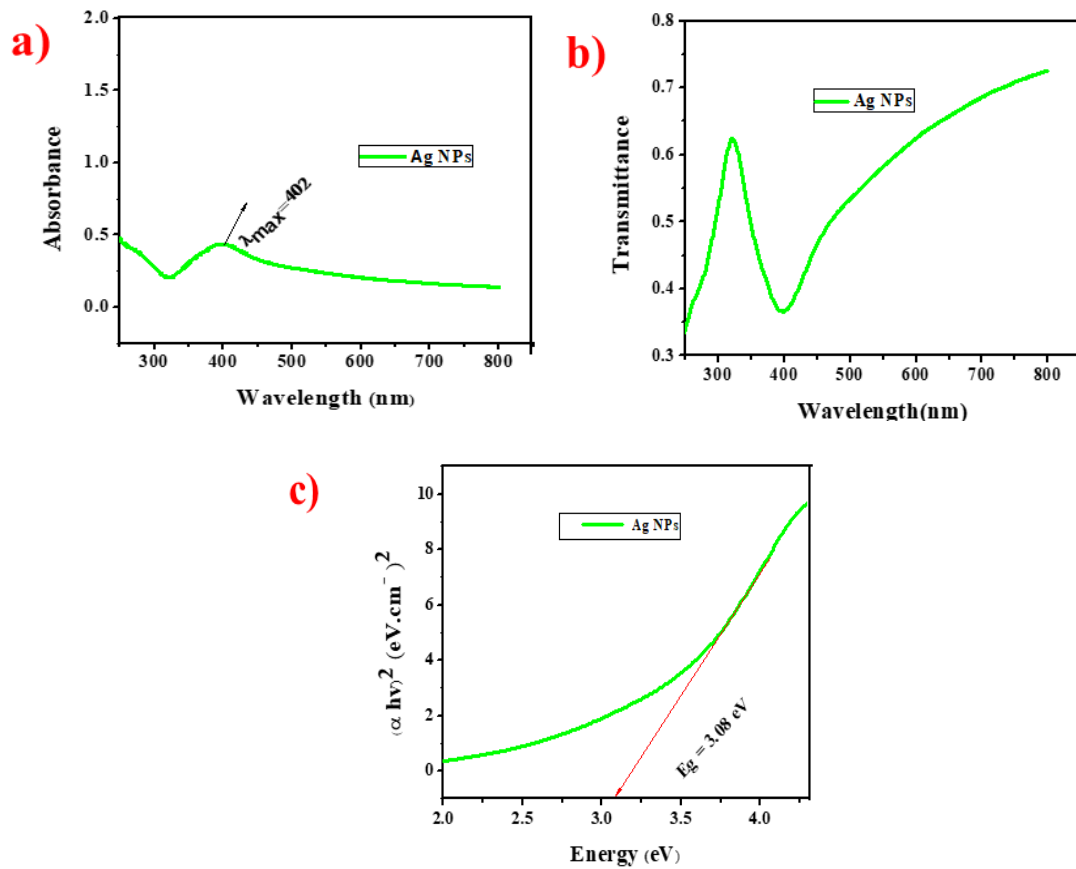


Fig. 4. a) Wavelength versus absorbance plot, (b) wavelength versus transmittance (c) energy bandgap of Ag Ns.

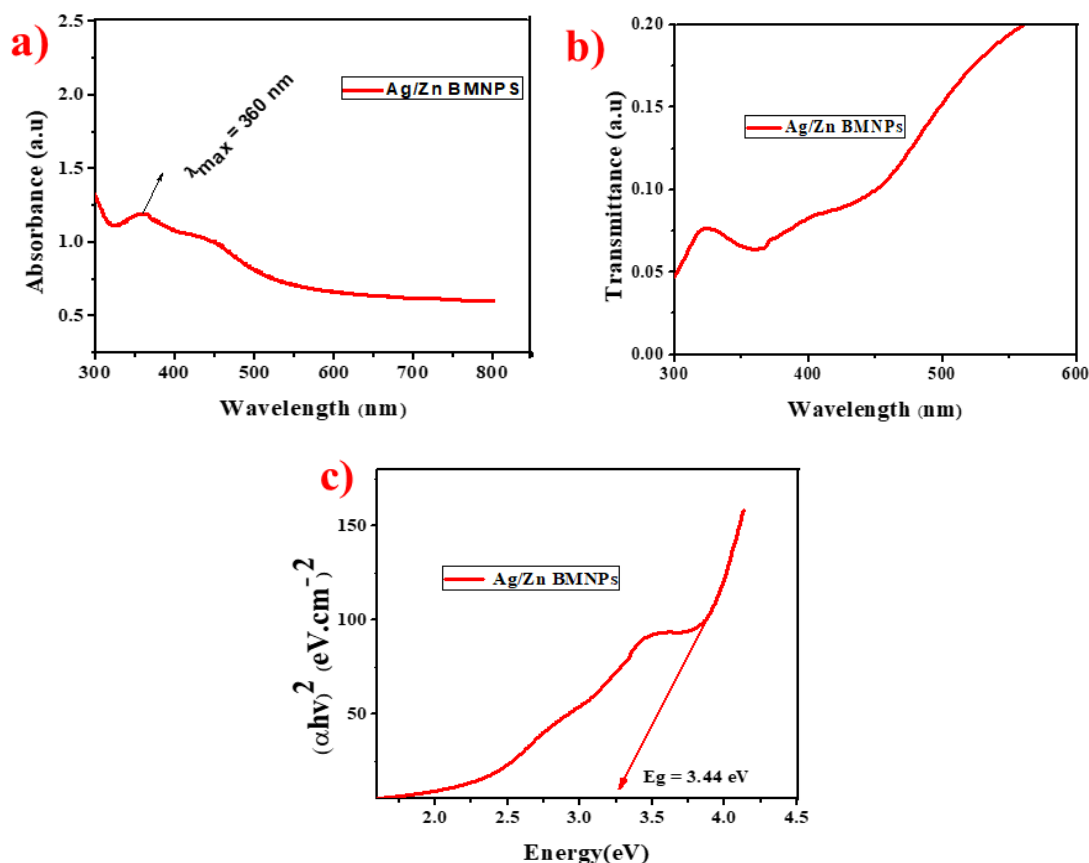


Fig. 5. Wavelength versus absorbance plot, (b) wavelength versus transmittance (c) energy bandgap of Ag/Zn BMNs.

Figure 6 depicts the comparison of absorption spectra for Ag Ns and Ag/Zn BMNs. The bandgap energy for the synthesized nanoparticles was determined according to equation 5, while the plots were shown in Figure 4(c) and Figure 5(c) which fitted with the calculated bandgap energy (equation 6) using the maximum wavelength of absorbance and tabulated in table 4.

The energy band gaps:

$$(\alpha hv)^2 = \kappa(hv - E_g) \quad (5)$$

where  $\alpha$  = absorbance coefficient,  $h$  = Planck constant,  $v$  = Frequency of incident radiation,  $k$  = Constant,  $hv$  = photon Energy,  $E_g$  = Band gap energy.

$$E_g = \frac{1240}{\lambda_{\max}} \quad (\text{eV}) \quad (6)$$

$$\alpha = 2.303 \times \frac{A}{t} \quad (7)$$

where  $A$  = absorbance and  $t$  is the thickness of the cuvette (1 cm)

The maximum absorption is observed at 360 nm and 402 nm for Ag/Zn BMNs and Ag Ns, respectively. The corresponding optical band gap energy values calculated using equation 6 and the results were found to be 3.44 eV and 3.08 eV for Ag/Zn BMNs and Ag Ns, respectively (Figure 6). As reported in literature, the UV-vis peaks for Ag nanoparticles appeared in the range of 400 nm- 450 nm [14,18], similar with our results. Regarding the bandgap energy plots, it was

found to decrease as the particle size of NPs decreases, the properties of nanoparticles being enhanced. It can be noticed that the bandgap energy for the synthesized Ag Ns is lower than that of Ag/Zn BMNs.

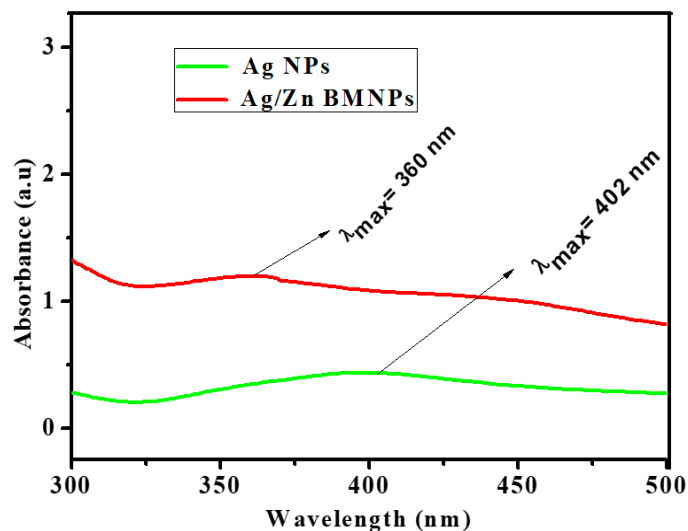


Fig. 6. The absorption spectra for Ag Ns and Ag/Zn BMNs.

Table 4. Calculated bandgap for Ag Ns and Ag/Zn BMNs.

Sample	$\lambda_{max}$ (nm)	The bandgap value (eV)
Ag NPs	402	3.08
Ag/Zn BMNs	360	3.44

### 3.2.3. Scanning Electron Microscopy (SEM) analysis

The morphological and textural features of Ag Ns and Ag/Zn BMNs were studied using SEM micrographs and presented in Figure 7(a,b). Irregular geometries and plate-like structures were noticed in both cases, the size of the particles being smaller in the case of monometallic Ag structures.

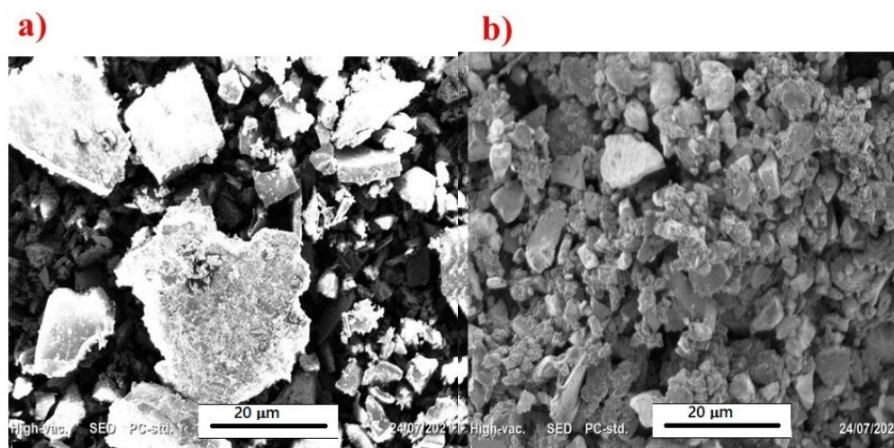


Fig. 7. The SEM micrographs of Ag/Zn BMNs (a) Ag Ns (b).

### 3.2.4. FTIR spectral analysis

The FT-IR spectra of synthesized mono and bimetallic structures were recorded at room temperature (range  $400\text{ cm}^{-1}$  to  $4000\text{ cm}^{-1}$ ). The absorption peaks were observed at  $3426\text{ cm}^{-1}$ ,  $2923\text{ cm}^{-1}$ ,  $1637\text{ cm}^{-1}$ ,  $1359\text{ cm}^{-1}$ ,  $1047\text{ cm}^{-1}$  and  $555\text{ cm}^{-1}$  with as depicted in Figure 8. The broadband located at  $3415\text{ cm}^{-1}$  is due to O-H stretching vibration mode. The peaks observed around the peak  $2923\text{ cm}^{-1}$  corresponds to asymmetric stretching of -C-H in  $\text{CH}_2$  and  $\text{CH}_3$  groups and -C-N group of secondary amines [19-21]. The carbonyl stretching peaks at  $1637\text{ cm}^{-1}$  are assigned to the tannins functional group [20]. The peak at  $1359\text{ cm}^{-1}$  shows C-N stretching of amide [22-24]. By comparing the spectra in Fig. 8, Ag/Zn BMNs showed small peak shifts compared to Ag Ns which confirm that the properties of Ag/Zn BMNPs are different from those of Ag Ns. In Table 6 are the main functional groups, confirming the presence of various phytochemicals of garlic plant extract as capping agent [25].

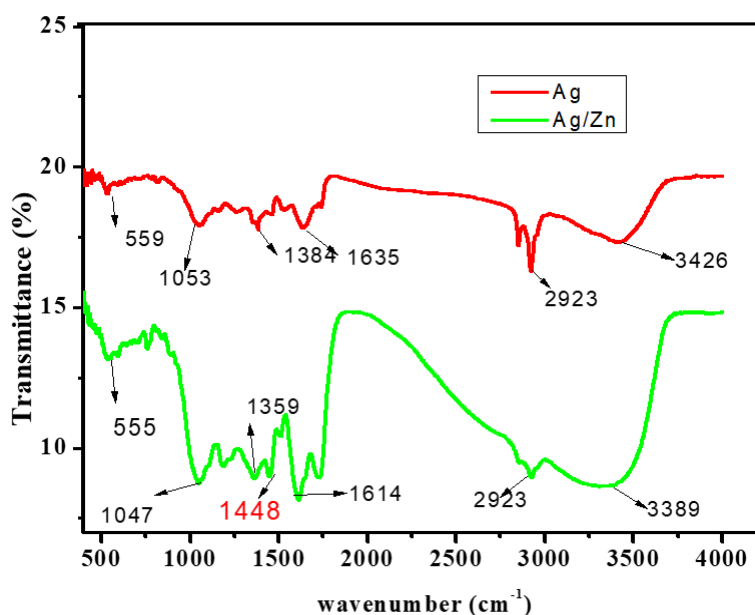


Fig. 8. FT-IR spectra of synthesized of Ag Ns and Ag/Zn BMNs.

Table 5. The characteristic of FT-IR for Ag Ns and Ag/Zn BMNs functional groups.

Wavenumber ( $\text{cm}^{-1}$ )	Functional group	Compound class	Intensity
3426	O-H stretching	Alcohol	Broad
2923	C-H stretching	Alkane	Medium
1637	C=C stretching	Aromatic	Strong
1359	C-H bend	Alkane	Weak
1047	C-O	Aliphatic amine	Strong
555	Cl-X	Chloro alkane	Weak

### 3.3. Evaluation of antibacterial activity

The antibacterial activities of synthesized materials towards the gram-negative bacterial species, (*E. coli* and *P. aeruginosa*) and gram-positive species (*S. pyogenes* and *S. aureus*) were investigated by the agar disc diffusion assay and presented in Figure 9 (a, b, c, d) for different concentrations of Ag and Ag/Zn BMNs. The quantitative results of antibacterial activities were tabulated in the table 7 and table 8, respectively. According to literature, the mechanism of the biocidal action of synthesized Ag Ns involves disruption of the cell membrane of bacterial species and finally causing the death of pathogens [26-28]. In our experiment, the size of the inhibition

zone was different with respect to the type of pathogens, the concentration and type of the synthesized nanostructures.

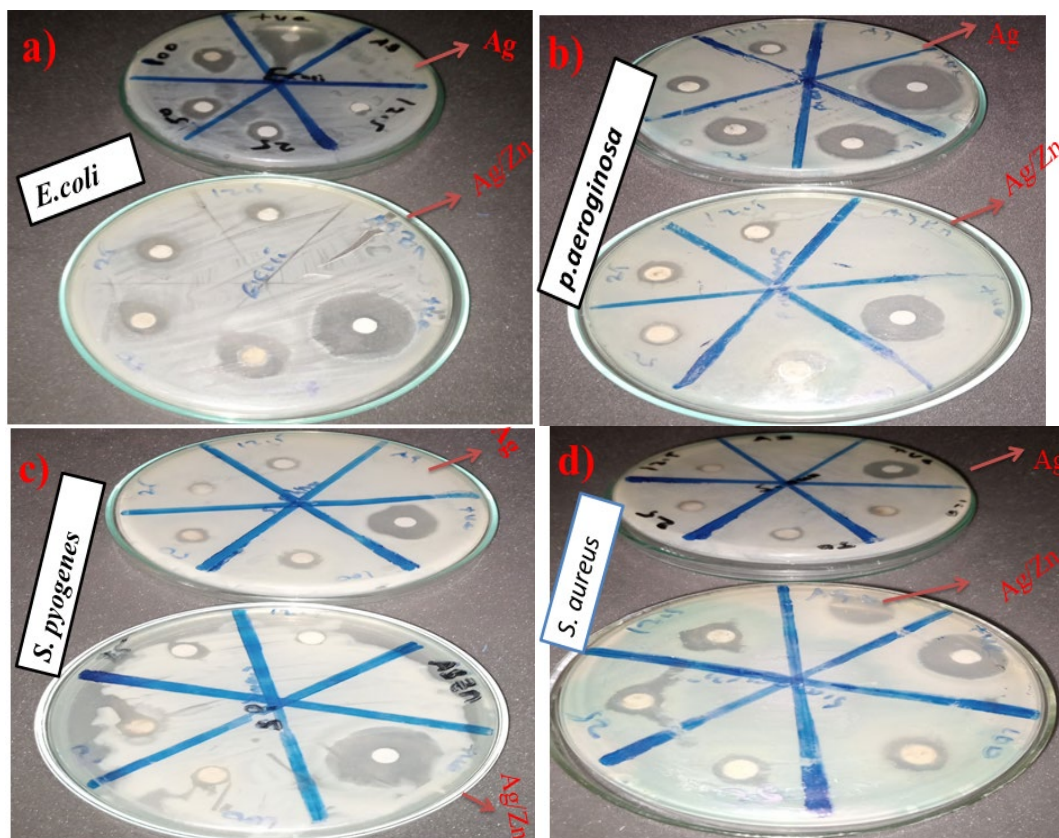


Fig. 9. Antibacterial activities of Ag Ns and Ag/Zn BMNs against (a) *E. coli*, (b) *P. aeruginosa*, (c) *S. pyogenes* and (d) *S. aureus*.

In this study, the gram-negative bacteria show more susceptibility to nanostructured-mediated toxicity as compared to gram-positive bacteria (Figure 10), because gram-negative bacteria possess a thinner layer of peptidoglycan-based cell membrane [29,30].

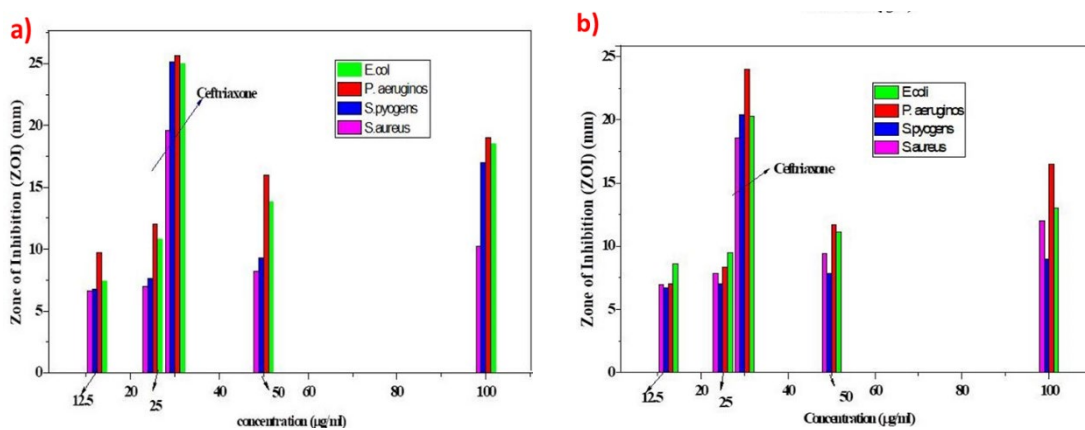


Fig. 10. The zone of inhibition of (a) Ag Ns, (b) Ag/Zn BMNs and Ceftriaxone (+ve control) against bacterial strains *E. coli* and *P. aeruginosa* (gram negative) and *S. pyogenes* and *S. aureus* (gram positive).

Table 6. Zones of inhibition of Ag Ns with different concentrations and Ceftriaxone (+ve control) against different bacterial strains.

Sample	Concentration (µg/m)	Zone of inhibition (mm)			
		Gram-negative		Gram-positive	
		<i>E. coli</i>	<i>P. aeruginosa</i>	<i>S. pyogenes</i>	<i>S. aureus</i>
Ag NPs	100.0	18.50 ± 0.87	19 ± 0.32	17.83 ± 0.25	10.27 ± 0.50
	50.0	13.83 ± 0.14	16 ± 0.10	9.33 ± 0.76	8.23 ± 0.06
	25.0	10.8 ± 0.15	12 ± 0.50	7.67 ± 0.15	7 ± 0.44
	12.5	7.4 ± 0.60	9.17 ± 0.56	6.77 ± 0.25	6.6 ± 0.40
Ceftriaxone (+ve control)	30.0	25 ± 0.80	25.67 ± 0.31	25.17 ± 0.02	19.63 ± 0.27

Table 7. Zone of inhibition of Ag/Zn BMNPs with different concentrations and Ceftriaxone (+ve control) against different bacterial species.

Sample	Concentration (µg/mL)	Zone of inhibition (mm)			
		Gram-negative sp		Gram-positive sp	
		<i>E. coli</i>	<i>P. aeruginosa</i>	<i>S. pyogenes</i>	<i>S. aureus</i>
Ag/Zn BMNPs	100.0	13 ± 0.74	16.5 ± 0.87	8.97 ± 0.56	12 ± 0.14
	50.0	11.1 ± 0.98	11.67 ± 0.31	7.83 ± 0.25	9.43 ± 0.11
	25.0	9.5 ± 0.20	8.33 ± 0.29	7.03 ± 0.21	7.83 ± 0.40
	12.5	8.63 ± 0.51	7 ± 0.30	6.7 ± 0.17	6.93 ± 0.93
Ceftriaxone (+ve control)	30.0	20.25 ± 0.02	24 ± 1.0	20.37 ± 1.30	18.53 ± 0.29

By comparing antibacterial activities of Ag and Ag/Zn BMNs against selected bacterial strains (*E. coli*, *P. aeruginosa*, *S. pyogenes* and *S. aureus*), we can notice that Ag Ns present better inhibition activities toward the selected bacterial species than Ag/Zn BMNs, as presented in Figure 11 (a-d). Based on previous findings in literature, it was expected for bimetallic structures to be more reactive due to synergistic effect of both metals [8]. Of course, the bioactivity strongly depends on the size, morphology and crystalline features, which derived from the experimental conditions such as reagent concentrations, pH and temperature.

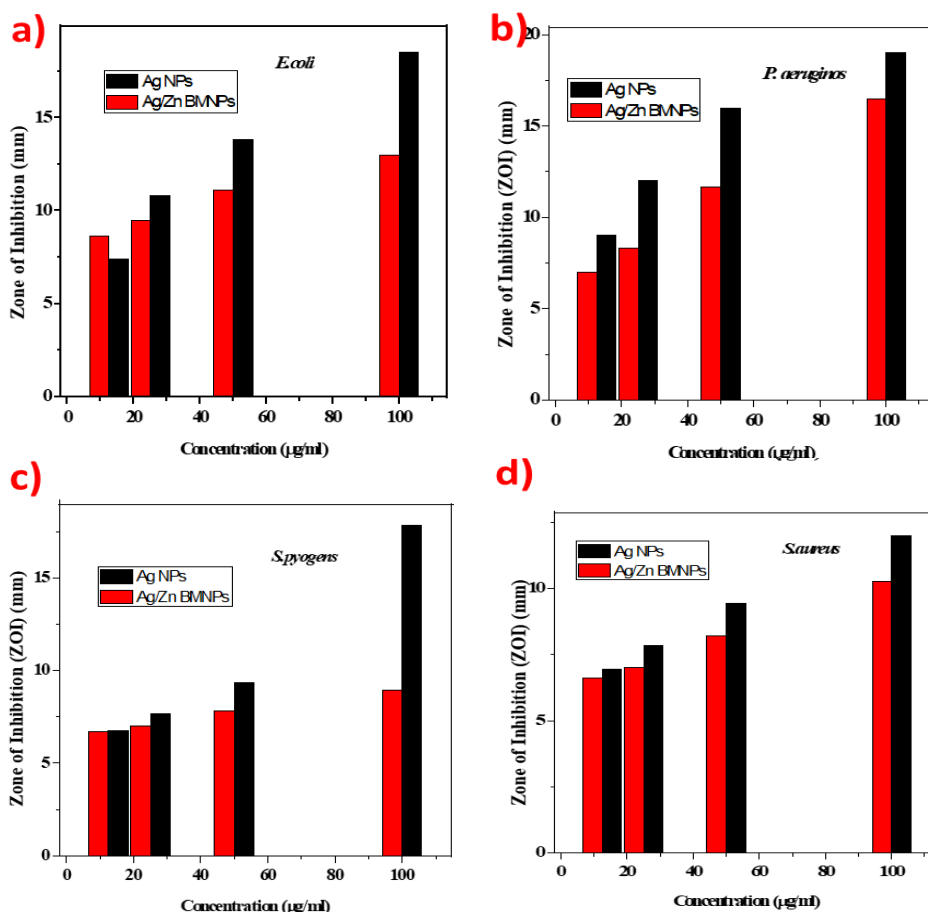


Fig. 11. Comparing the inhibition activities of Ag Ns and Ag/Zn BMNs against *E. coli*, *P. aeruginosa*, *S. pyogenes* and *S. aureus*.

#### 4. Conclusions

Mono and bimetallic Ag and Ag/Zn BMNs were synthesized via the green synthesis method by using garlic plant extract. The phytochemical screening of the garlic (*Allium sativum* L.) extract revealed the presence of flavonoids, tannins, terpenoids, glycosides, phytosterols, saponins and phenols. These biomolecules are responsible for the reduction and stabilization of Ag Ns and Ag/Zn BMNs. The synthesized nanostructures were characterized by XRD, UV-Vis, SEM, and FT-IR techniques. The XRD result confirmed the cubic crystalline structure for both Ag and Ag/Zn BMNs with average crystallite sizes of 9.31 nm and 17.47 nm respectively. The maximum absorption wavelengths were recorded at 360 nm and 402 nm for Ag/Zn BMNs and Ag Ns, while the energy bandgap values were found to be 3.44 eV and 3.08 eV, respectively. The morphology of synthesized nanostructures was evidenced by SEM micrographs, confirming the lower particle size of mono metallic Ag NPs compared to Ag/Zn BMNs. The FTIR features confirms the capping surface created by the phytochemicals contained in *Allium sativum* L. extract. The antibacterial tests of synthesized conducted against the gram-negative (*E. coli* and *P. aeruginosa*)

and gram-positive species (*S. pyogenes* and *S. aureus*) revealed superior efficiency of Ag Ns compared to Ag/Zn BMNPs, as revealed by disc diffusion assay. The best antibacterial results were obtained with respect to *P. aeruginosa* strain.

## References

- [1] Islam, F.; Shohag, S.; Uddin, M.J.; Islam, M.R.; Nafady, M.H.; Akter, A.; Mitra, S.; Roy, A.; Emran, T.B.; Cavalu, S. *Materials* 2022, 15, 2160; <https://doi.org/10.3390/ma15062160>
- [2] Bhattacharya, T.; Das, D.; Borges e Soares, G.A.; Chakrabarti, P.; Ai, Z.; Chopra, H.; Hasan, M.A.; Cavalu, S. *Processes* 2022, 10, 426; <https://doi.org/10.3390/pr10020426>
- [3] Desalegn, T., Ravikumar, C.R., Murthy, H.C.A. *Appl. Nanosci.* 2021, 11, 535-551; <https://doi.org/10.1007/s13204-020-01620-7>
- [4] Cavalu, S.; Antoniac, I.V.; Fritea, L.; Mates, I.M.; Milea, C.; Laslo, V.; Vicas, S.; Mohan, A. *Journal of Adhesion Science and Technology* 2018, 32, 22, 2509-2522; <https://doi.org/10.1080/01694243.2018.1490067>
- [5] Cavalu, S.; Banica, F.; Simon, V., Akin, I.; Goller, G. *International Journal of Applied Ceramic Technology* 2014, 11, 2, 402-411; <https://doi.org/10.1111/ijac.12075>
- [6] Murthy, H.C.A., Desalegn, T., Kassa, M., Abebe, B. & Assefa, T. *J. Nanomaterials* 2020, 1-12; <https://doi.org/10.1155/2020/3924081>
- [7] Abebe, B., Murthy, H.C.A., Zereffa, E.A., Adimasu, Y. *Inorganic and Nano-Metal Chemistry* 2020, 50, 1-12; <https://doi.org/10.1080/24701556.2020.1814338>
- [8] Sumbal, Nadeem A., Naz, S., Ali, J., Mannan, A., Zia, M. *Biotechnology Reports*, 2019, 22, e00338; <https://doi.org/10.1016/j.btre.2019.e00338>
- [9] Cavalu, S.; Fritea, L.; Brocks, M.; Barbaro, K.; Murvai, G.; Costea, T.O.; Antoniac, I.; Verona, C.; Romani, M.; Latini, A.; Zilli, R.; Rau, J.V. *Materials* 2020, 13, 2077; <https://doi.org/10.3390/ma13092077>
- [10] Shahin, P., Faranak, H., Farideh, A., & Murthy, H. C. A. *Green Chem. Lett. Rev.*, 2021, 14:3, 518-532; <https://doi.org/10.1080/17518253.2021.1963492>
- [11] Manickam, S., Perumal, V., Shanmugam S., Ramasamy R. *Langmuir*, 2018, 34:46, 13897-13904; <https://doi.org/10.1021/acs.langmuir.8b02096>
- [12] Latif-ur-Rahman, Afzal Shah, Rumana Qureshi, Sher Bahadar Khan, Abdullah M. Asiri, Anwar-ul-Haq Ali Shah, Muhammad Ishaq, Mohammad Saleem Khan, Suzanne Kay Lunsford, Muhammad Abid Zia. *Advances in Materials Science and Engineering*, 2015, Article ID 638629, 8 pages; <https://doi.org/10.1155/2015/638629>
- [13] Desalegn, T., Murthy, H.C.A, Ravikumar, C.R., Nagaswarupa H.P. *J. Nanostruct*, 2021, 11(1): 81-94; <https://doi.org/10.22052/JNS.2021.01.010>
- [14] Murthy, H.C.A., Desalegn Zeleke. T., Ravikumar, C.R., Anil Kumar, M.R. *Mater. Res. Express* 2020, 7 (5) 055016; <https://doi.org/10.1088/2053-1591/ab9252>
- [15] Nadeem, A., Naz, S., Ali, J. S., Mannan, A., Zia, M. *Biotechnology Reports*, 2019, 22, e00338; <https://doi.org/10.1016/j.btre.2019.e00338>
- [16] Kumar, MRA., Abebe, B., Nagaswarupa, HP., Murthy, HCA, Ravikumar, CR., Sabir, FK. *Sci. Rep.* 2020, 10(1); <https://doi.org/10.1038/s41598-020-58110-7>
- [17] Rostek, A., Loza, K., Heggen, M., Epple, M. *RSC advances*, 2019, 9(46), 26628-26636; <https://doi.org/10.1039/C9RA05117A>
- [18] Kumar, M.R.A., Ravikumar, C.R., Nagaswarupa, H.P., Purshotam, B., Gonfa, B., Murthy, H.C.A., Sabir, F.K., Tadesse, S. *J. Environ. Chem. Eng.* 2019, 7 (6); <https://doi.org/10.1016/j.jece.2019.103468>
- [19] Karnib, M., Holail, H., Olama, Z., Kabbani, A., Hines, M. *Int. J. Curr. Microbiol. App. Sci*, 2013, 2(4), 20-30.
- [20] Gul R, Jan SU, Faridullah S, Sherani, S., Jahan N. *The Scientific World Journal*, 2017, 2017:1-7; <https://doi.org/10.1155/2017/5873648>

- [21] Jha, A. K., Prasad, K. International Journal of Green Nanotechnology: Physics and Chemistry, 2010, 1(2), P110-P117; <https://doi.org/10.1080/19430871003684572>
- [22] Vorokh, A. S. Scherrer formula: estimation of error in determining small nanoparticle size. Nanosystems: Physics, Chemistry, Mathematics, 2018, 9(3), 364-369; <https://doi.org/10.17586/2220-8054-2018-9-3-364-369>
- [23]. Taran, M., Rad, M., & Alavi, M. Appl Pharm Sci, 2016, 6(11), 094-099; <https://doi.org/10.7324/JAPS.2016.601115>
- [24] Cinta-Pinzaru, S.; Cavalu, S.; Leopold, N.; Petry, R.; Kiefer, W. Raman and surface-enhanced Raman spectroscopy of tempyo spin labelled ovalbumin. Journal of Molecular Structure 2001, 565, 225-229; [https://doi.org/10.1016/S0022-2860\(00\)00930-3](https://doi.org/10.1016/S0022-2860(00)00930-3)
- [25] Ricci, A., Olejar, K. J., Parpinello, G. P., Kilmartin, P. A., Versari, A. Applied Spectroscopy Reviews, 2015, 50(5), 407-442; <https://doi.org/10.1080/05704928.2014.1000461>
- [26] Khan, M. A., Khan, T., Nadhman, A. Adv. Colloid Interface Sci. 2016, 234, 132-141; <https://doi.org/10.1016/j.cis.2016.04.008>
- [27]. Lakshmi, N. D. M., Mahitha, B., Madhavi, T., Sushma, N. J. International Journal of Scientific & Engineering Research, 2015 6(2), 287-290; <https://doi.org/10.18311/jnr/2020/24381>
- [28] Silhavy, T. J., Kahne, D., Walker, S. Cold Spring Harbor perspectives in biology, 2010, 2(5), a000414; <https://doi.org/10.1101/cshperspect.a000414>
- [29] Desalegn, T., Murthy, H C A., Limeneh Yeshaneh A. Ethiopian Journal of Science and Sustainable Development, 2021, 8 (1), 1-12; <https://doi.org/10.20372/ejssdastu.v8.i1.2021.265>
- [30] Ormanci, O., Akin, I., Sahin, F., Yucel, O., Simon, V., Cavalu, S., Goller, G. Mater. Sci. Eng. C 2014, 40, 16–23; <https://doi.org/10.1016/j.msec.2014.03.041>